Available online at www.sciencedirect.com
SCIENCE DIRECT®
Journal of Power Sources 140 (2005) 331–339
JOURNAL OF POWER SOURCES
www.elsevier.com/locate/jpowsour

Numerical study of a flat-tube high power density solid oxide fuel cell Part I. Heat/mass transfer and fluid flow

Yixin Lu[1], Laura Schaefer*, Peiwen Li[2]

Department of Mechanical Engineering, University of Pittsburgh, Benedum Engineering Hall, Pittsburgh, PA 15261, USA

Received 29 July 2004; accepted 26 August 2004

Abstract

The flat-tube high power density (HPD) solid oxide fuel cell (SOFC) is a new design developed by Siemens Westinghouse, based on their formerly developed tubular type SOFC. It has increased power density, but still maintains the beneficial feature of secure sealing of a tubular SOFC. In this paper, a three-dimensional numerical model to simulate the steady state heat/mass transfer and fluid flow of a flat-tube HPD-SOFC is developed. In the numerical computation, governing equations for continuity, momentum, mass, and energy conservation are solved simultaneously. The highly coupled temperature, concentration and flow fields of the air stream and the fuel stream inside and outside the different chambers of a flat-tube HPD-SOFC are investigated. The variation of the temperature, concentration and flow fields with the current output is studied. The heat/mass transfer and fluid flow modeling and results will be used to simulate the overall performance of a flat-tube HPD-SOFC, and to help optimize the design and operation of a SOFC stack in practical applications.

Keywords: Flat-tube; High power density; Solid oxide fuel cell; Simulation; Heat and mass transfer; Fluid flow

1. Introduction

1.1. Fuel cell operation

Like any other fuel cells, a SOFC produces electrical power through an electrochemical reaction. Working at a high operating temperature (600–1000 °C), a SOFC is a clean, quiet, and highly efficient power generation device [1,2]. Due to the high working temperature, a SOFC can be combined with other power generation systems (e.g., gas turbines) to achieve high overall electrical power generation efficiency [3,4]. Another attractive feature of a SOFC is its ability to directly utilize hydrocarbon fuels, whereas some other types of fuel cells have to rely on a clean supply of hydrogen for their operation. The high operating temperature makes a SOFC possible to reform hydrocarbons within the system either indirectly in a discrete reformer or directly in the anode of the cell. SOFC technology is now considered to be one of the most promising stationary power generating methods for the future. Studies of heat/mass transfer and electrochemical performance on SOFCs currently are focused on tubular and planar structured models [5–9]. However, with the development of the new configuration of HPD-SOFC, a specific modeling study for this new type is very necessary.

A SOFC basically consists of three major components, a porous air electrode (cathode), a porous fuel electrode (anode), and an electrolyte, which is gas tight but conductive to oxide ions. Oxygen at the cathode accepts the electrons from the external circuit to form oxide ions. The oxide ions conduct through the electrolyte to the anode-electrolyte interface and combine with the hydrogen to form water. The electrons released in this process flow through the external circuit back to the cathode. The reactions in a hydrogen-consuming SOFC

* Corresponding author. Tel.: +1 412 624 9793; fax: +1 412 624 4846.
E-mail addresses: yil5@pitt.edu (Y. Lu), laschaef@engr.pitt.edu (L. Schaefer), pel1+@pitt.edu (P. Li).
[1] Tel.: +1 412 624 9766; fax: +1 412 624 4846.
[2] Tel.: +1 412 624 3096; fax: +1 412 624 4846.

0378-7753/$ – see front matter © 2004 Elsevier B.V. All rights reserved.
doi:10.1016/j.jpowsour.2004.08.036

Nomenclature

A	constant in Eq. (13)
A_{fuel}	cross-sectional area for the fuel stream (m^2)
A_{air}	cross-sectional area for the air stream (m^2)
B	constant in Eq. (13)
c	mole fraction of species at the inlet
c_p	heat capacity ($J\,kg^{-1}\,^\circ C$)
$D_{i,m}$	mass diffusivity of gas i in a gas mixture ($m^2\,s^{-1}$)
e^-	electron
EMF	electromotive force (V)
F	Faraday's constant 96486.7 ($C\,mol^{-1}$)
ΔG	Gibbs free energy change ($J\,mol^{-1}$)
ΔG°	standard Gibbs free energy change ($J\,mol^{-1}$)
ΔH	enthalpy change of the reaction ($J\,mol^{-1}$)
H_2	hydrogen
H_2O	water
i	local current density ($mA\,cm^{-2}$)
i_l	constant in Eq. (13)
i_n	constant in Eq. (13)
i_0	constant in Eq. (13)
I	total current (A)
k	thermal conductivity ($W\,m^{-1}\,^\circ C^{-1}$))
O_2	oxygen
O^{2-}	oxide ion
P	pressure (Pa)
q	heat production for a discretized mesh volume (W)
$\dot{q}$	volumetric heat source ($W\,m^{-3}$)
Q	total heat production (W)
r	resistance (Ω)
R	universal gas constant 8.31434 ($J\,mol^{-1}\,K$)
ΔS	entropy change of the reaction ($J\,mol^{-1}\,K$))
S_m	source term in the concentration governing equation ($mol\,s^{-1}$)
T	temperature
u	velocity ($m\,s^{-1}$)
U	inlet velocity of the fluids ($m\,s^{-1}$)
Y	mole fraction of species

Greek letters

η	utilization percentage
μ	dynamic viscosity ($kg\,m^{-1}\,s^{-1}$))
ρ	density ($kg\,m3^{-1}$)

Subscripts

air	air stream
fuel	fuel stream
H_2	hydrogen
H_2O	water vapor
ia	air stream inlet
if	fuel stream inlet
O_2	oxygen

Superscripts

r	chemical reaction
j	Joule
irr	irreversibility

are:

$$\text{Cathode}: \quad \tfrac{1}{2}O_2 + 2e^- \Rightarrow O^{2-} \tag{1}$$

$$\text{Anode}: \quad H_2 + O^{2-} \Rightarrow H_2O + 2e^- \tag{2}$$

$$\text{Overall}: \quad H_2 + \tfrac{1}{2}O_2 \Rightarrow H_2O \tag{3}$$

The free energy change of the overall chemical reaction (Eq. (3)) is converted to electrical energy via an electrical current. The electrical potential or the electromotive force (EMF) between the cathode and the anode is related to the Gibbs free energy change of the chemical reaction, the temperature T at the reaction site, and the partial pressures of the participating species:

$$\text{EMF} = \frac{-\Delta G^\circ{}_{H_2O}}{2F} + \frac{RT}{2F} ln\left(\frac{p_{H_2} p_{O_2}^{1/2}}{p_{H_2O}}\right) \tag{4}$$

where p_{H_2O} and p_{H_2} are the partial pressures of water vapor and hydrogen at the anode-electrolyte interface. p_{O_2} is the partial pressure of oxygen at the interface of the cathode and the electrolyte. T is the temperature at the interface of the anode and the electrolyte, and $\Delta G^\circ_{H_2O}$ is the standard Gibbs free energy change of the electrochemical reaction, which is a function of temperature at the interface of the anode and the electrolyte.

1.2. SOFC configurations

There are currently two major types of SOFCs, planar and tubular. In a planar SOFC, the cathode, anode, electrolyte, and interconnection (Fig. 1) are all laminated in a plate-type structure. The major advantages of a planar SOFC are manufacturing ease and high current density.

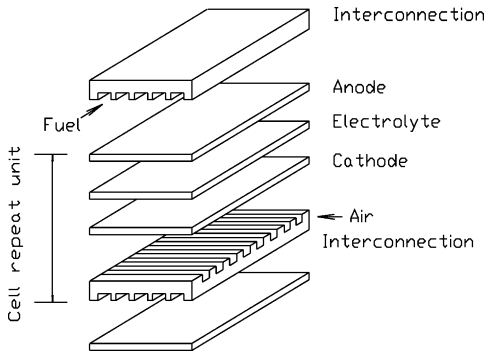

Fig. 1. Configuration of a planar SOFC.

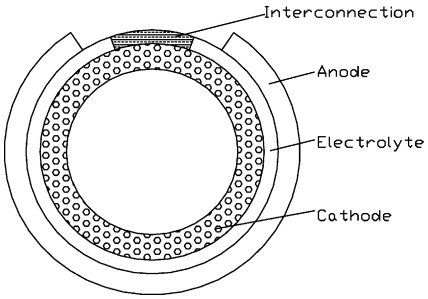

Fig. 2. Cross-section of a tubular SOFC.

The tubular SOFC design is a concept developed by Westinghouse (currently Siemens Westinghouse) in the 1980s. It consists of same components as a planar SOFC, namely, a cathode, an anode, an electrolyte, and an interconnection, but in a different structure, as seen in Fig. 2. Air and fuel are provided in the arrangement as shown in Fig. 3. Due to the geometry, tubular designs have a self-sealing structure, which improves thermal stability and eliminates the need for the highly thermal-resistant sealants that are required in the planar configuration [10].

In the last 15 years, Siemens Westinghouse has made significant progress in tubular SOFC development. Up to November 2001, the demonstration unit of a tubular SOFC and micro gas turbine system had worked continually for more than 18,000 h, and achieved an efficiency of 52%. By varying the working pressure of the SOFC, the performance of this system can still improve. It is expected that the efficiency of a hybrid system can approach up to 70% [3,11].

In the near future, a goal for the tubular SOFC is to develop economically acceptable systems. It is expected that the capital costs can be lowered through advancement in cell

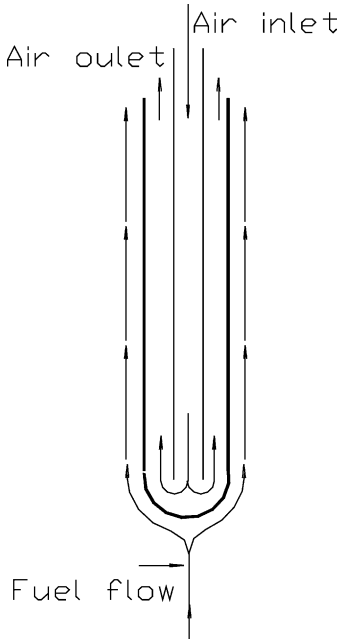

Fig. 3. Air and fuel delivery for a tubular SOFC.

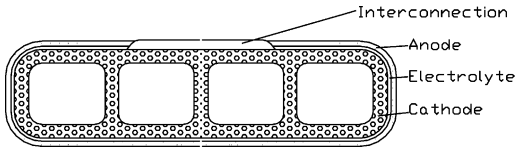

Fig. 4. Cross-section of a four-chamber flat-tube SOFC.

manufacturing and cell design. An increase in power density is a major technical contribution to further cut costs. So far, the research for increasing the power density has produced the cell design of a flat-tube HPD-SOFC. This is an innovation that enhances the power density and yet retains the feature of secure sealing [3,11,12]. The current modeling work described in this paper is aimed at simulating the flow, heat and mass transfer, and the electrochemical performance throughout the new structure of the HPD-SOFC.

1.3. Flat-tube HPD-SOFC configuration

A flat-tube solid oxide fuel cell has the same components and working principles as that of a tubular solid oxide fuel cell. It is comprised of a cathode, an anode, an electrolyte, and an interconnection in a flat-tube structure (Fig. 4). The air and fuel delivery method in this study is also similar to that of a tubular SOFC (Fig. 5). The difference between a tubular solid oxide fuel cell and a flat-tube solid oxide fuel cell is the geometry and the structure of the cell stack. The cross-section of the flat-tube type SOFC looks like a flattened tube. Multiple ribs may be built into the cathode (air electrode) side, and the airflow area is divided into several chambers. Each chamber has its own air introducing tube. The number of chambers is decided by how many ribs are constructed. The ribs are ion conductive and can serve as a short cut for the inner ion conducting circuit, which will reduce the cell resistance and hence increase the cell power density [3]. Meanwhile the flat-tube shape makes it possible to keep the secure sealing feature of a tubular SOFC. In a practical flat-tube SOFC stack, many cells are mounted in a bundle. Most of the single cells work under the same/similar environment of temperature and concentration of gas species as shown in the typical single domain in Fig. 6. Because of the symmetry of arrangement,

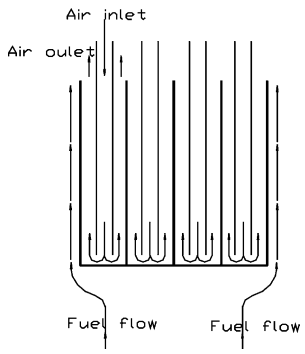

Fig. 5. Air and fuel flow arrangement for a four-chamber flat-tube SOFC.

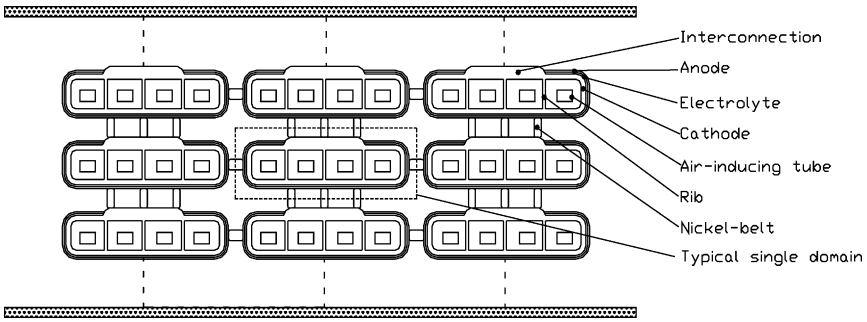

Fig. 6. Orientation of a flat-tube SOFC in a cell bundle.

it can be assumed that there are no flow velocity and heat and mass fluxes across the domain boundary. This will greatly simplify the analysis. A single flat-tube solid oxide fuel cell is symmetric along the centerline. The left half of a flat-tube solid oxide fuel cell has same structures for fluid flow and heat/mass transfer as that of right half due to the symmetry. For simplicity, only left half part is considered in the study. Three-dimensional heat/mass transfer and fluid flow inside and outside different chambers are investigated. In our near future work, currently in progress, the overall performance and stack optimization of a flat-tube SOFC, which could have arbitrary number of chambers, will be studied based on the present numerical modeling and results.

2. Heat/mass transfer and fluid flow model

In a chamber of a flat-tube SOFC stack, fuel and air flow in respective channels. The electrochemical reaction occurs at the interface of anode and electrolyte, and reactants (hydrogen and oxygen) are consumed along the cell. The electrochemical reaction heat and irreversibility heat is released at the reaction site. Since electrical current is conducted in cell tube including ribs, Joule heat is released in these solid parts.

For a single flat-tube SOFC with four chambers, the left-most and second left chambers in Fig. 5 are considered to be two typical chambers. For a flat-tube SOFC with more than four chambers, the behaviors of the other inner chambers are similar to that of the second left chamber. The cell stack and fuel/air stream flow patterns of a whole cell are schematically illustrated in Figs. 4 and 5, respectively. The cross-section and fuel/air stream flow pattern of the left-most chamber is shown in Figs. 7 and 8, respectively. The cross-section of second left (inner) chamber is shown in Fig. 9.

The fluids in SOFC channels have multiple components. In an air channel, the fluid consists of oxygen and nitrogen. In a fuel channel, it consists of hydrogen and water vapor. The heat/mass transfer and fluid flow are coupled with each other.

The governing equations for flow, temperature and species concentration for this Three-dimensional case are:

$$\nabla \cdot (\rho u) = 0 \tag{5}$$

$$\nabla \cdot (\rho u u) = -\nabla p + \nabla \cdot (\mu \nabla u) \tag{6}$$

$$\nabla \cdot (\rho u c_p T) = \nabla \cdot (k \nabla T) + \dot{q} \tag{7}$$

$$\nabla \cdot (\rho u Y_i) = \nabla \cdot (\rho D_{i,m} \nabla Y_i) + S_m \tag{8}$$

Since the arrangement of cells (Fig. 6) is symmetric in a cell bundle, the domain borders between cell stacks for heat/mass transfer are considered to be adiabatic. The boundary along the ribs assumed to be adiabatic for heat/mass transfer. The boundary conditions for the chemical species at the interfaces between the active solid and gas streams must satisfy the mass flux balances by following equations:

$$\frac{M_{H_2}}{A_{H_2}} = -D_{H_2,H_2O}\rho_{H_2}\nabla Y_{H_2} \tag{9}$$

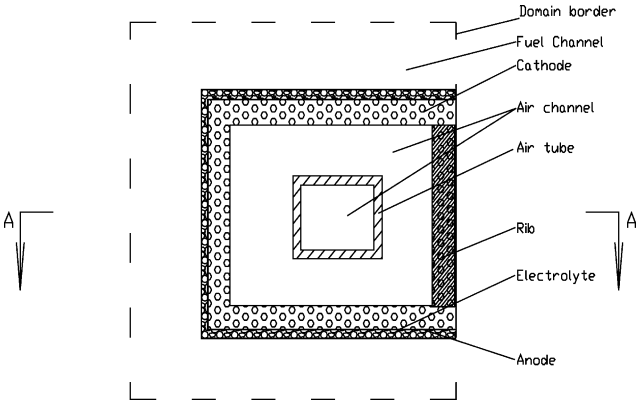

Fig. 7. Computational domain of the left-most chamber.

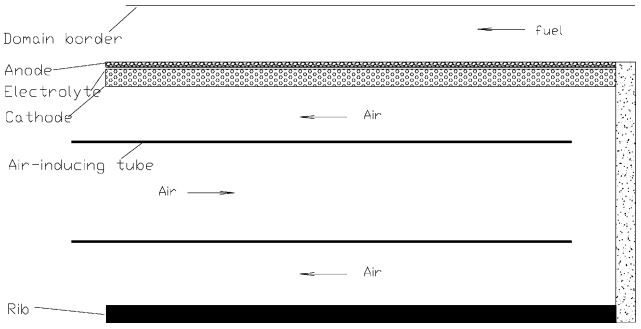

Fig. 8. Air and fuel flow arrangement for the left-most chamber (A–A section in Fig. 7).

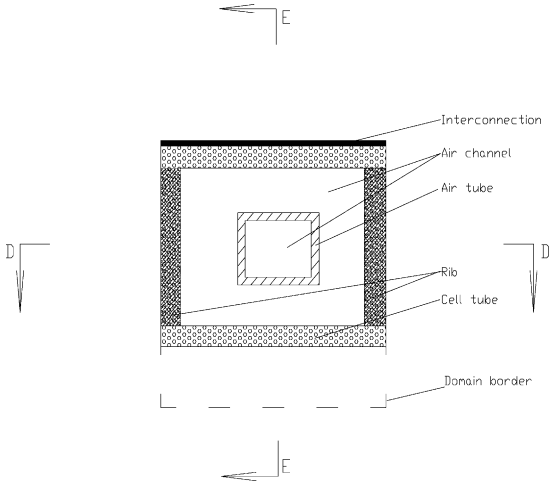

Fig. 9. Computational domain of the second left (inner) chamber.

$$\frac{M_{H_2O}}{A_{H_2O}} = -D_{H_2O,H_2}\rho_{H_2O}\nabla Y_{H_2O} \tag{10}$$

$$\frac{M_{O_2}}{A_{O_2}} = -D_{O_2,N_2}\rho_{O_2}\nabla Y_{O_2} \tag{11}$$

where A_{H_2}, A_{H_2O} and A_{O_2} are the active interface area of solid and hydrogen, water vapor, and oxygen respectively. M_{H_2}, M_{H_2O} and M_{O_2} are consumed amounts for respective species calculated as following:

$$M_{H_2} = m_{H_2}\frac{I}{2F} \tag{12}$$

$$M_{H_2O} = m_{H_2O}\frac{I}{2F} \tag{13}$$

$$M_{O_2} = m_{O_2}\frac{I}{4F} \tag{14}$$

The velocities at the borders between cell stacks are assumed to be zero. The inlet velocity of the fuel and air are determined based on the current output of the fuel cell:

$$U_{fuel} = \left(\frac{I}{2F\eta_{H_2}c_{H_2}A_{fuel}}\right)\frac{RT_{if}}{P_{if}} \tag{15}$$

$$U_{air} = \left(\frac{I}{4F\eta_{O_2}c_{O_2}A_{air}}\right)\frac{RT_{ia}}{P_{ia}} \tag{16}$$

where U is the inlet velocity, F is Faraday's constant, η_{O_2} and η_{H_2} are the oxygen and hydrogen utilization factor respectively, A_{fuel} and A_{air} are the inlet cross-area of the fuel and air stream respectively, c_{H_2} and c_{O_2} are the inlet molar fractions of the fuel and air, P_{if} and T_{if} are the pressure and the temperature of the fuel at the inlet, and P_{ia} and T_{ia} are the pressure and the temperature of the air at the inlet. The inlet temperatures of the fuel and air are set as 800 and 600 °C, respectively. The inlet fuel composition is 90% hydrogen and 10% water vapor, and the inlet air stream composition is 21% oxygen and 79% nitrogen. The total heat produced in an operating fuel cell consists of three parts including chemical reaction heat, irreversibility heat and Joule heat. The chemical reaction heat is calculated based on the electrochemical reaction heat through the thermodynamic relationship by Eq. (17) and considered to be applied evenly where electrochemical reaction occurs.

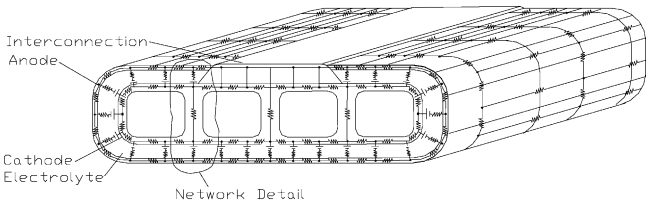

Fig. 10. Electric circuit network of a discretized cell stack.

$$Q^r = \frac{(\Delta H - \Delta G)I}{2F} \tag{17}$$

where, ΔH is the enthalpy change and ΔG is the Gibbs free energy change, which is, ideally, converted to electrical power. Q^r is the thermal energy released at the interface of the anode and electrolyte. Joule heat is produced due to electric current conduction through cell stack materials. The Joule heat is calculated by:

$$q^j = i^2 r \tag{18}$$

where i is the local current and r the local resistance of the discretized material of the anode, electrolyte and cathode, as shown in Figs. 10 and 11. The Joule heat and irreversibility heat is then obtained through the simulation of the network

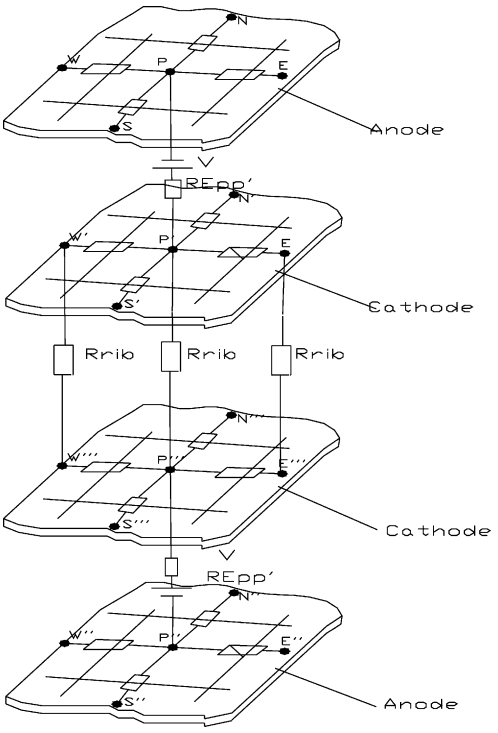

Fig. 11. Sample of the discretized network circuit near a rib (network detail in Fig 10).

Table 1
Constants for Eq. (20) in this simulation

Constants for a high temperature SOFC	
A (V)	0.04
B (V)	0.002
i_n mA cm^{-2}	2
i_0 mA cm^{-2}	0.02
i_l mA cm^{-2}	670

Table 2
The dimension of single chamber computation domain

Constants for a high temperature SOFC	cm
Cell length	50
Domain width	2.0
Domain height	2.0
Chamber width	1.5
Chamber height	1.5

circuit of the discretized cell stack as shown in Fig. 10 using a commercial software.

In the Circuit network, the voltage sources and the resistances are given by the following equations:

$$V = EMF - \Delta V \tag{19}$$

$$\Delta V = Aln\left(\frac{i+i_n}{i_0}\right) - Bln\left(1-\frac{i+i_n}{i_l}\right) \tag{20}$$

$$r = \rho\frac{l}{A} \tag{21}$$

where, i is local current density. Constant A, B, i_n, i_0, and i_l are given in Table 1. In Eq. (20), $A\ln[(i+i_n)/i_0]$ is the activation loss known as Tafel equation and $-B\ln[1-(i+i_n)/i_l]$ is the concentration loss [13].

The heat of irreversibility is calculated by:

$$q^{irr} = i\left(Aln\left(\frac{i+i_n}{i_0}\right) - B\ln\left(1-\frac{i+i_n}{i_l}\right)\right) \tag{22}$$

The properties of gases are from the Perry's Chemical Engineers' Handbook [14]. The thermal properties of the solid materials of the cell components are from the literature [7,15]. The major dimensions used in the computation are given in Table 2.

3. Results and discussions

Simulations have been conducted to investigate the temperature, velocity, and pressure fields. Some typical results are shown and discussed in this section. In most simulations, the computation domains are discretized by $65 \times 65 \times 475$, and the numerical convergence and results are stable.

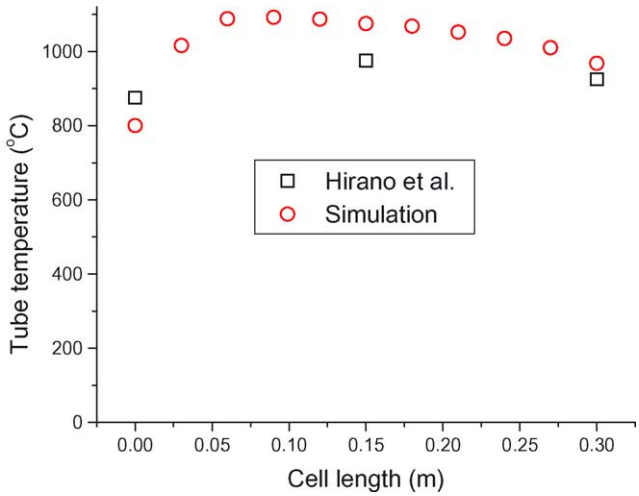

Fig. 12. Comparison of the cell tube temperature distribution between the simulation result of a flat-tube SOFC (most left side) and the experimental data of a tubular SOFC.

3.1. Temperature profiles

The 3-D temperature field of the computation domain is obtained through numerical computation. Because experimental temperature measurement is rather difficult in a SOFC, there is no published experimental data of the temperature for a flat-tube SOFC. Experimental data for the tubular SOFC is also very rare. Only a few experimental temperature data are available from the work by Hirano et al. [16] for the temperatures at two ends and middle part of a tubular SOFC tube. Fig. 12 shows the tube temperature distribution of left end of the cell tube (Fig. 4) for a 30 cm long flat-tube SOFC in the case of 400 mA cm^{-2} of current density. The experimental temperature data of a tubular SOFC from the work of Hirano et al. [16] are also plotted in Fig. 12. The tube temperature distribution along the flat-tube SOFC tube agrees with the trend observed by Hirano et al. for a tubular SOFC. The cell tube has higher temperatures in the middle part than in two ends of the tube along a SOFC. For further comparison, more experimental data for flat-tube or tubular SOFCs are expected in the future, and will be used for verification of the numerical simulation.

3.1.1. Local temperature distribution for a left-most chamber

For the case of a current density of 400 mA cm^{-2} and fuel and air utilization percentages of 85 and 15%, respectively, the temperature profile of the cross-section A–A (shown in Figs. 7 and 8) is given in Fig. 13. The air in the air introducing tube is heated gradually by the air flowing toward the

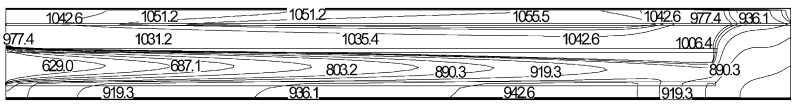

Fig. 13. Cross-sectional temperature field of the left-most chamber (current density: 400 mA cm^{-2}).

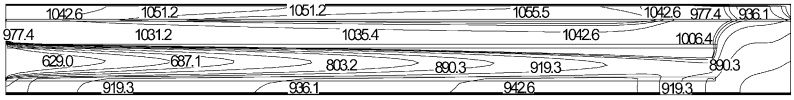

Fig. 14. Cross-sectional temperature field of the left-most chamber (current density: 300 mA cm^{-2}).

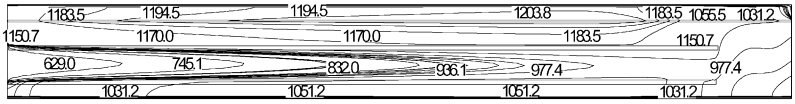

Fig. 15. Cross-sectional temperature field of the left-most chamber (current density: 500 mA cm^{-2}).

outlet of the air chamber, which also obtains heat from the heat generating cell components. Because of the large thermal conductivity and relatively small velocity of the fuel, the fuel stream in the fuel channel is heated quickly by the cell tube. The air temperature in the air channel near the rib is slightly lower than the air temperature in the other places in the channel. This is because the electrochemical reaction does not occur in the rib. The largest temperature gradients occur at the inlet tube wall of the air introducing tube and the inlet of fuel stream. The air heating effect inside the air introducing tube changes with variations in the dimensions of the air introducing tube, because the variation will change the velocity ratio of the air inside and outside the introducing tube.

The current density determines the power output and the fuel and air consumption, as well as the inlet fuel and air velocity. Therefore, the inlet fuel and air velocity and the temperature fields vary with the current density. Figs. 14 and 15 show the two temperature fields for two different current densities of 300 and 500 mA cm^{-2}. From Figs. 14 and 15, it can be seen that the average temperatures of the air and fuel stream increase with the current density, and that the temperature distribution features in the air and fuel channels do not change significantly.

3.1.2. Local temperature distribution of the inner chamber

Fig. 16 shows the temperature field of the E–E section of an inner chamber. In this section, the temperature gradient in the vertical direction of the cell tube is large. Along the cell tube, the major temperature gradients are found at the inlet and outlet of the fuel and air stream. The tube temperature distribution along the active tube surface only changes slightly except the area near the fuel stream inlet. Fig. 17 shows the temperature field of D–D section of an inner chamber. Compared to the temperature field of a similar cross-section of the left-most chamber, the overall temperature is lower due to the less active surfaces. Considering that in this study the radioactive heat transfer effect is not considered, the practical temperature fields should be more uniform, especially in the vertical direction of the fuel and air stream, although the radioactive heat transfer effect is not expected to greatly change the overall temperature field along the cell tube. Since the airflow rate decreases with the reacted amount and the active surface area are different between chambers, the temperature also shows difference between chambers (Fig. 18). Through proper airflow distribution of the chambers, the temperature differences between the left-most chambers and inner chambers might be alleviated, which can reduce the thermal stress of material.

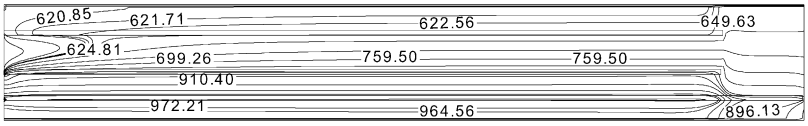

Fig. 16. E–E sectional (Fig. 9) temperature field of the inner chamber (current density: 400 mA cm^{-2}).

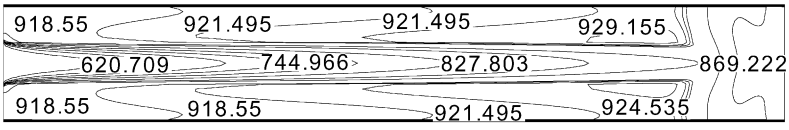

Fig. 17. D–D sectional (Fig. 9) temperature field of the inner chamber (current density: 400 mA cm^{-2}).

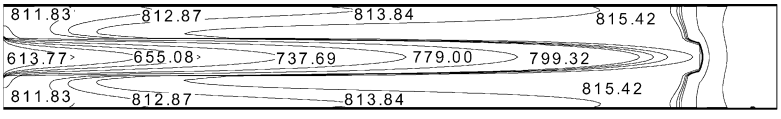

Fig. 18. D–D sectional (Fig. 9) temperature field of the inner chamber without flow control (current density: 400 mA cm^{-2}).

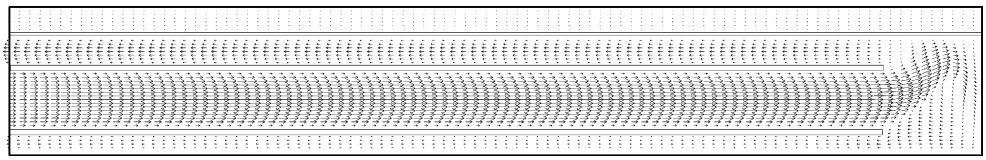

Fig. 19. Velocity field of the left-most chamber A–A cross-section.

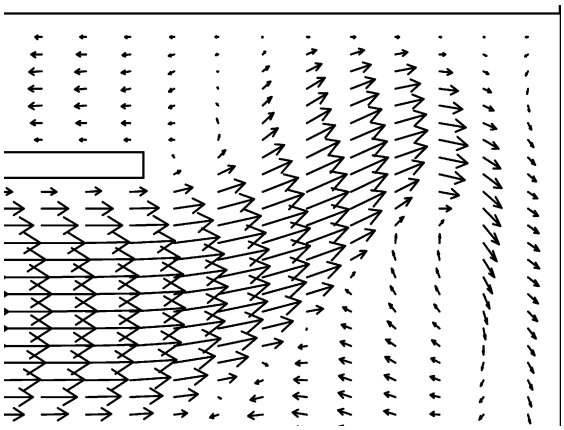

Fig. 20. Velocity profile at the air introducing tube corner in the A–A cross-section.

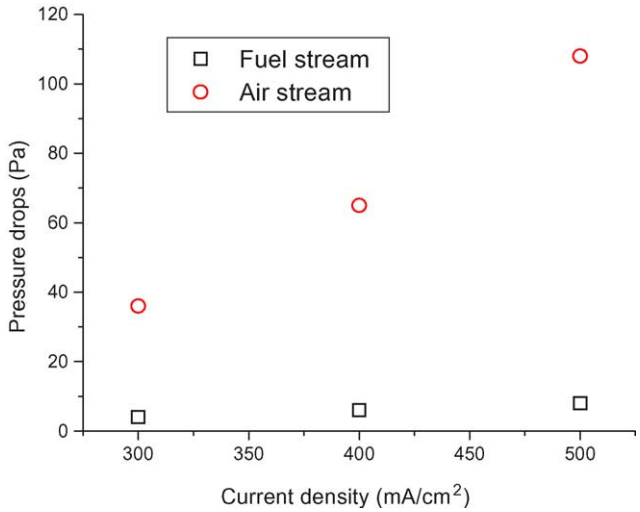

Fig. 22. Pressure drops of the fuel and air stream in the left-most chamber for different current densities.

Virtually, airflow distribution is easy to perform, which can reduce any complexity of temperature control through other measures.

3.2. Velocity profiles

The 3-D velocity field of the computation domain is also obtained. For the case of a current density of 400 mA cm^{-2} and fuel and air utilization percentages of 85 and 15%, respectively, the velocity profile of the cross-section A–A (shown in Figs. 7 and 8) is given in Fig. 19. It is seen from Fig. 19 that air flows in the introducing tube through the entrance, turns back at the closed end of the air channel, and then flows along the air channel and gives its oxygen to the cathode when it is near the exit of the air channel. Fig. 20 is a magnification of the detail of the airflow in the returning area. The fuel enters the fuel channel from the closed end of the cell stack and flows toward the open end of the cell stack along the fuel channel, which occurs around the cell stack. At the inlet of air introducing tube, the mean velocity of the air increases slightly due to the increasing temperature. The mean velocities distribution in the other parts of the air-introducing tube and the air channel outside the air-introducing tube are quite stable due to the stable temperature fields. Compared to the fuel velocity, the mean velocity of the air is much larger. This is because the air quantity is supplied several times as needed and the oxygen concentration in the air is also relatively low. The velocity distribution of the fuel stream is shown separately in Fig. 21. The dimensions of the cell stack and air-introducing tube affect the fuel velocity and the velocity of the air inside and outside the air-introducing tube, and hence the temperature distribution. This dimensional optimization will be discussed together with the overall performance simulation in our future work.

The power output affects the velocity and temperature field significantly due to the different heat generation in the fuel cell. In the case of a current density of 400 mA cm^{-2} and fuel and air utilization percentages of 85 and 15%, respectively, the airflow and fuel flow pressure drops are 66 and 5 Pa, respectively, in the left-most chamber. These pressure drops vary with the power output and cell stack dimensions. The pressure drops of the fuel and air stream, for different current densities are shown in Fig. 22. For the inner chamber, the pressure drops have similar values. From this result, we can conclude that the pressure along the cell will not affect the EMF significantly.

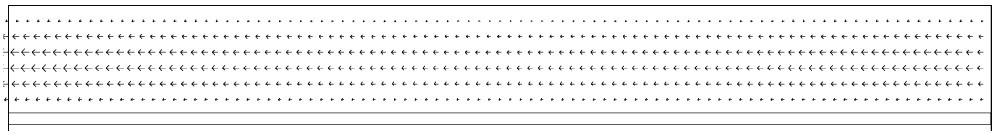

Fig. 21. Fuel stream velocity profile of the left-most chamber of the A–A cross-section.

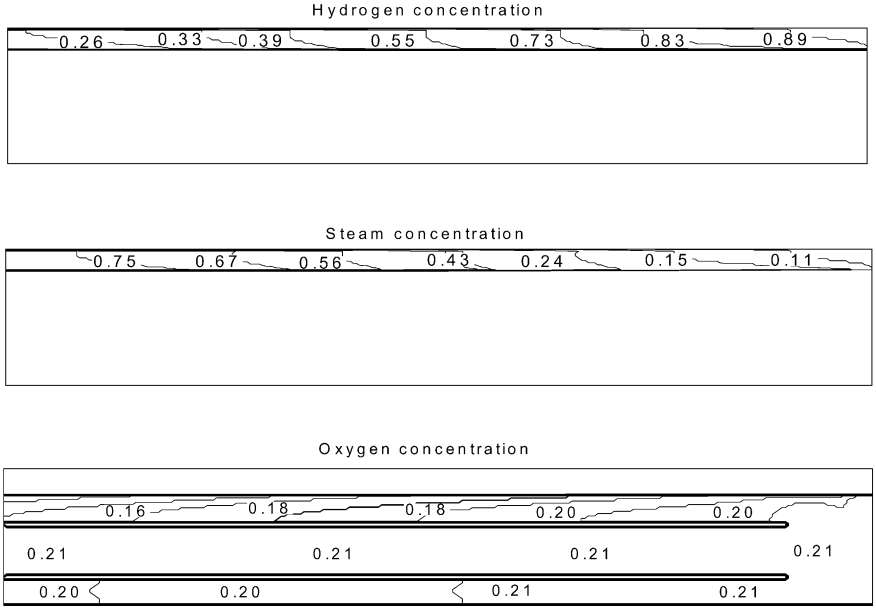

Fig. 23. Selected figures from the simulation for the species' mole fraction contours in the A–A cross-section of the left-most chamber.

3.3. Concentration profiles

Fig. 23 shows the gas species' mole fraction contours for the cross-section A–A of the left-most chamber under the same operating conditions discussed in Figs. 14 and 19–21. The hydrogen mole fraction contour shows that the hydrogen concentration decreases from the closed end to the open end along the cell due to the consumption by the electrochemical reaction. The slight difference of contour line implies the temperature's effect on the species' diffusivities. The contour of oxygen mole fraction shows similar behavior. The molar fraction of oxygen decreases along the flow direction. We can see from the third plot in Fig. 23 that in the cross-section A–A, the oxygen consumption in the air path near the ribs is less than that near the active surface and the contour line is flattened because of no electrochemical reaction occurring at the ribs. These species' concentration contour figures also imply that if the laminar flow assumption in this study is valid in practical applications, the mass transport resistance does greatly affect the cell performance. The species' concentration contour plots of the inner chambers have the same features as the left-most chamber.

4. Conclusions

Modeling and numerical simulation for the three-dimensional heat and fluid flow in a flat-tube high power density (HPD) solid oxide fuel cell is performed. The heat transfer and fluid flow behaviors of the fuel and air streams in a representative chamber are discussed. This work provides an important basis for an overall simulation and optimization of the flat-tube HPD-SOFC.

References

[1] S.C. Singhal, Solid State Ionics 152–153 (2002) 405–410.
[2] A.B. Stambouli, E. Traversa, Renewable Sustainable Energy Rev. 6 (2002) 433–455.
[3] S.C. Singhal, Solid State Ionics 135 (2000) 305–313.
[4] R.A. George, J. Power Sources 86 (2000) 134–139.
[5] S. Ahamed, C. McPheeters, R. Kumar, J. Electrochem. Soc. 138 (1991) 2712–2718.
[6] S. Campanari, J. Power Sources 92 (2001) 26–34.
[7] J.R. Ferguson, J.M. Fiard, R. Herbin, J. Power Sources 58 (1996) 109–122.
[8] S. Nagata, A. Momma, T. Kato, Y. Kasuga, J. Power Sources 101 (2001) 60–71.
[9] K.P. Recknagle, R.E. Williford, L.A. Chick, D.R. Rector, M.A. Khaleel, J. Power Sources 113 (2003) 109–114.
[10] L. Carrette, K.A. Friedrich, U. Stimming, Fuel cells–fundamentals and applications, Fuel Cells 1 (2001) 5–39.
[11] N.F. Bessette, B.P. Borglum, H. Schichl, D.S. Schmidt, Siemens SOFC technology on the way to economic competitiveness, Power J. (Magazine of the Siemens Power Generation Group) (2001) 10–13.
[12] S.D. Vora, D. Collins, Small-scale low cost solid oxide fuel cell power systems, Fuel Cell Annu. Rep. (2003) 18–20.
[13] J. Larminie, A. Dicks, Fuel Cell System Explained, John Wiley & Sons, 2000.
[14] R.H. Perry, D.W. Green, J.O. Maloney, Perry's Chemical Engineers' Handbook, seventh ed., McGraw-Hill, New York, 1997.
[15] M. Iwata, T. Hikosaka, M. Morita, T. Iwanari, K. Ito, K. Onda, Y. Esaki, Y. Sakaki, S. Nagata, Solid State Ionics 132 (2000) 297–308.
[16] A. Hirano, M. Suzuki, M. Ipponmatsu, J. Electrochem. Soc. 139 (1992) 2744–2751.